ELSEVIER

Introducing C phase in additively manufactured Ti-6Al-4V: A new oxygen-stabilized face-centred cubic solid solution with improved mechanical properties

H. Wang [1,&], Q. Chao [2,&], X.Y. Cui [1], Z.B. Chen [1,3,*], A.J. Breen [1], M. Cabral [1], N. Haghdadi [4], Q.W. Huang [1], R.M. Niu [1], H.S. Chen [1], B. Lim [1], S. Primig [4], M. Brandt [5], W. Xu [2,*], S.P. Ringer [1,*], X.Z. Liao [1,*]

[1] Australian Centre for Microscopy & Microanalysis, and School of Aerospace, Mechanical and Mechatronic Engineering, The University of Sydney, Sydney, NSW 2006, Australia
[2] School of Engineering, Deakin University, Waurn Ponds, VIC 3216, Australia
[3] Research Institute for Advanced Manufacturing, Department of Industrial and Systems Engineering, The Hong Kong Polytechnic University, Hong Kong, China
[4] School of Materials Science & Engineering, UNSW Sydney, Kensington, NSW 2052, Australia
[5] Centre for Additive Manufacturing, School of Engineering, RMIT University, Melbourne, VIC 1000, Australia

An oxygen-rich face-centred cubic (FCC) Ti phase was engineered in the microstructure of a Ti-6Al-4V alloy via additive manufacturing using laser powder bed fusion. Designated 'C', this oxygen-rich FCC phase has a lattice parameter of 0.406 nm and exhibits an orientation relationship with the parent α' phase as follows: $(0001)_{\alpha'}//\{111\}_{C}$, and $\langle 1\bar{2}10\rangle_{\alpha'}$ $//\langle 1\bar{1}0\rangle_{C}$. We propose that the formation of the C phase is facilitated by the combined effect of thermal gradients, deformation induced by the martensitic transformation, and local O enrichment. This enables an in-situ phase transformation from the hexagonal close-packed α' phase to the C phase at elevated temperatures. Our density functional theory calculations indicate that oxygen occupancy in the octahedral interstices of the FCC structure is energetically preferred to corresponding sites in the α' phase. The in-situ mechanical testing results indicate that the presence of the FCC phase significantly increases the local yield strength from 1.2 GPa for samples with only the α' phase to 1.9 GPa for samples comprising approximately equal volume fractions of the α' and FCC phases. No loss of ductility was reported, demonstrating great potential for strengthening and work hardening. We discuss the formation mechanism of the FCC phase and a pathway for future microstructural design of titanium alloys by additive manufacturing.

Keywords: FCC Ti; Additive manufacturing; Interstitial strengthening; Mechanical properties

Introduction

Titanium and its alloys – especially Ti-6Al-4V – exhibit a remarkable combination of high specific strength, and excellent corrosion resistance such that they are widely used in critical applications ranging from aerospace to biomedical implants. Their capacity for plastic deformation is limited, in large part, by the hexagonal close-packed (HCP) nature of the low-temperature α phase. Speculation that a face-centred cubic (FCC) form of Ti can be stabilized at room temperature goes back several decades [1–13]. Multiple controversies have emerged from these propositions [1–3,5,12], such that today it is widely agreed that the FCC forms of Ti are either intermetallic

* Corresponding authors.
E-mail addresses: Chen, Z.B. (zi-bin.chen@polyu.edu.hk), Xu, W. (wei.xu@deakin.edu.au), Ringer, S.P. (simon.ringer@sydney.edu.au), Liao, X.Z. (xiaozhou.liao@sydney.edu.au).
[&] These authors contributed equally to this work.

1369-7021/ https://doi.org/10.1016/j.mattod.2022.10.026

compounds such as hydrides, or highly localized and defect-stabilized metastable phase segments that can occur when Ti alloys are subjected to electron beam or ionized radiation [11].

A persistent feature of these debates has been the considerable uncertainty about the role of interstitial elements such as H, C, N and O. Moreover, O is known to impart a dramatic strengthening effect at low concentrations in Ti alloys and this can quickly become an embrittling effect at higher O concentrations [14–16]. For this reason, precise control of interstitial content is a significant cost consideration in conventional metallurgical processing of Ti alloys. The advent of metal additive manufacturing (AM) brings highly non-equilibrium processing such that alloys are subjected to abrupt and complex thermal and stress gyrations that are far from those encountered in conventional metallurgical processing. The large thermal gradients and their rapid rate of change coupled with the potential for introducing interstitials into the built part through the feedstock materials (e.g. powder or wire) and/or via the build-chamber environment [17–20] creates a wholly new process dynamic [18,21–23] affecting the strength, ductility, fatigue life, and other critical materials properties [20,24,25]. As a general example, these process dynamics have recently been shown to enable the formation of ordered oxygen complexes that contribute simultaneous enhancement of strength and ductility in high-entropy alloys [26]. Here, we explore the potential for interstitial oxygen to be purposefully integrated into the AM build to dramatically improve the mechanical properties through a novel phase transformation wherein an FCC form of Ti can be stabilized.

Our research has been focussed on the benchmark dual-phase Ti-6Al-4V which demonstrates excellent manufacturability by various AM processes [17,23,25,27]. The microstructure of the Ti-6Al-4V alloy is comprised of the high-temperature body-centered cubic (BCC) β phase ($Im\bar{3}m$, a = 0.3190 nm) [28–29] and the low temperature HCP α phase (P63/mmc, a = 0.2925 nm, c = 0.4670 nm) [28–31]. A metastable martensitic version of the HCP phase is also widely reported—known as the α′ phase (P63/mmc, a = 0.2931 nm, c = 0.4681 nm) [28,30,32]: this phase can achieve yield strengths over 1300 MPa, but the total tensile elongation is below the minimum threshold of ~10% recommended for critical structural applications [28]. Recently an ultrafine-grained α + β microstructure was achieved in the as-built condition via AM using laser powder bed fusion (L-PBF): the layer thickness, laser power, and focal offset distance were controlled to achieve a target thermal profile of the melt pool such that martensite decomposition occurred [32]. This AM dual-phase α/β Ti-6Al-4V alloy exhibited an outstanding yield strength of 1100 MPa with total tensile elongation of 11.4 % [32].

The high chemical affinity between Ti and the interstitial elements [33,34] is such that there is now extensive literature on their incorporation in conventionally processed Ti alloys. The formation of titanium hydride [2,12,35], titanium nitride [36], titanium carbide [36] and titanium oxide [23] have all been reported. The presence of these intermetallic compounds is linked to a low tolerance for crack initiation and propagation [30,32,37]. Here it is noted that the state of bonding in these compounds is distinctly non-metallic and ranges from strongly ionic to covalent [38]. In AM-built Ti–6Al–4V parts, the tolerance levels for O typically range between ~0.6 to ~1.2 at.%, without resulting in a dramatic reduction in ductility [39]. Dilute oxygen solutes cause an intense hardening effect in wrought pure titanium due to their interactions with dislocations [34]. Much less is known about how O incorporates with additively manufactured Ti alloys [17,32].

We report that the particular process dynamics of AM via L-PBF provide a window to stabilize a new FCC phase in Ti-6Al-4V. Advanced electron microscopy techniques were used to reveal the crystallographic and chemical details of the FCC phase, which is an interstitial O-containing solid solution. Density functional theory (DFT) calculations were performed to rationalize the formation mechanism of the oxygen-containing FCC phase. In-situ compression of micro-pillars in a scanning electron microscope (SEM) revealed that the presence of both FCC and HCP Ti phases generates a >60% higher ultimate strength than the HCP phase alone. Critically, no loss in the total tensile ductility was reported. Mechanical tests of bulk samples confirm that the strength and ductility of the FCC-bearing (~6 vol%) materials is strongly enhanced. We suggest that this creates a new process–property regime for this remarkable alloy and our findings may have wider applicability for opening a pathway to a new class of Ti-alloys containing substantial volume fractions of an FCC phase.

Results

Microstructure along the build direction

Fig. 1a presents a schematic diagram of the build coupon. The build direction is defined as the z direction and the x and y axes are perpendicular to this. Electron backscatter diffraction (EBSD) experiments were conducted on the cross-sectional y-z plane of the samples along the build direction. Figs. 1b-c present EBSD phase maps from a top layer (300 μm or 10 layers below the top surface), and a middle layer, respectively, as marked by the two rectangles in Fig. 1a. The top layer microstructure was dominated by the α′ phase (red, Fig. 1b) which exhibited an acicular morphology, consistent with similar observations of the as-built L-PBF Ti-6Al-4V microstructure and explained reasonably by the high local cooling rate expected in these locations [32]. In addition to the α′ phase, another phase (green, Fig. 1c) was unexpectedly observed in the middle layer. The diffraction pattern indexing was consistent with an FCC phase possessing a lattice parameter of 0.40 nm. The dimensions of the acicular-shaped α′ phase crystals in the middle layer were about the same as the dimensions of those in the top layer. The new FCC phase, designated C-phase, also exhibited an acicular shape. The volume fraction of the C-phase in the middle layer was ~3.7 vol.%. An extensive survey was undertaken using EBSD throughout different layers in the x-y plane along the build direction and it was revealed that the volume fraction of the FCC phase increased monotonically from 0.0 vol.% at the top layers to 6.6 vol.% at the bottom layers. The morphology and FCC structure of the C phase was further confirmed by transmission Kikuchi diffraction (TKD), transmission electron microscopy (TEM) bright-field (BF) imaging, and selected area electron diffraction (SAED), with typical images provided in Figs. 1d-e.

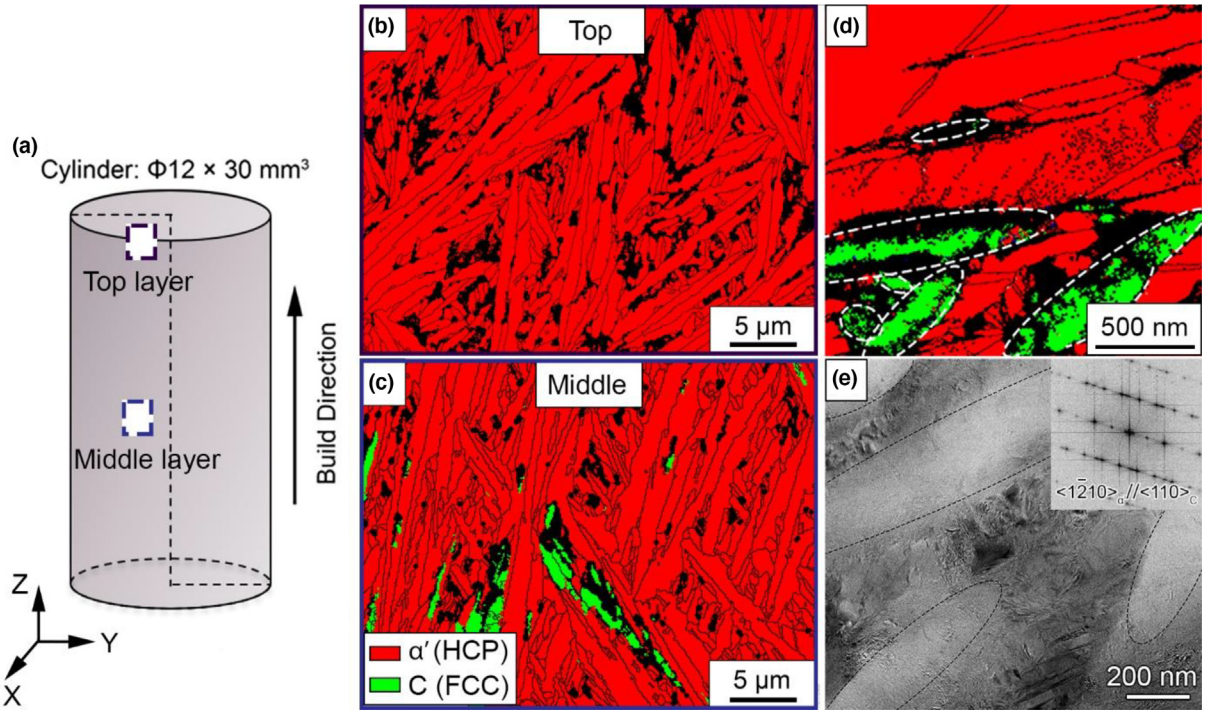

FIGURE 1

(a) A schematic diagram showing a top and a middle layer, marked with rectangles, from which the EBSD phase maps in (b) and (c) were recorded from, respectively, using a step size of 25 nm. The red and green colours represent the HCP α′ phase and the FCC C phase, respectively. The black areas were not indexed because of the high density of local defects. The average width and length of the acicular platelets of the α′ phase were ~0.9 μm and 8.1 μm, respectively. The widths and lengths of the C phase ranged between 0.4 μm to 1.4 μm (average value = 0.6 μm) and 0.8 μm to 10 μm (average value = 4.6 μm), respectively. (d) The TKD phase map reveals the morphology of the C phase. White dashed lines mark the phase boundaries. (e) The corresponding BF-TEM image taken from the same region as Fig. 1d. Black dashed lines mark the phase boundaries. The corresponding SAED is also provided (inset).

Structure and composition of the new C-phase

Scanning transmission electron microscopy (STEM) characterization was used to study the detailed microstructure of the C-phase. Figs. 2a-d provide high-angle annular dark-field (HAADF) images and their corresponding indexed fast Fourier transformation (FFT) patterns recorded along the $\langle 0\,0\,1\rangle_C$ and $\langle 0\,1\,1\rangle_C$ zone axes. Detailed analysis of the d-spacing ratios and the angles between different atomic planes confirmed the FCC crystal structure. A BF TEM image recorded from a dual-phase region is provided in Fig. 2e. The SAED pattern in Fig. 2f reveals the orientation relationship between the two phases as: $\langle 1\,\bar{2}\,1\,0\rangle_{HCP}//\langle 1\,\bar{1}\,0\rangle_{FCC}$ and $(0001)_{HCP}//\{111\}_{FCC}$, which is the most common orientation relationship observed in HCP to FCC phase transformations, generally [40]. This orientation relationship was further confirmed by TKD pole figures recorded from a two-phase region over a wider field of view, as shown in the Extended data Fig. S1.

Fig. 2g presents a STEM HAADF image recorded at a two-phase region along the $\langle 1\,\bar{2}\,1\,0\rangle_{HCP}$ //$\langle 1\,\bar{1}\,0\rangle_{FCC}$ zone axis, indicating that the $(0001)_{HCP}$ basal plane is precisely aligned with a $\{111\}_{FCC}$ close-packed plane. Both the SAED pattern provided in Fig. 2f, and the STEM image presented in Fig. 2g reveal that the $(0001)_{HCP}$ and $\{111\}_{FCC}$ planes have the same lattice plane spacing. Using the lattice parameters of the α′ phase as a reference (a = 0.293 ± 0.003 nm and c = 0.468 ± 0.003) [30], the atomic planar spacing of the $\{111\}_C$ is the same as that of $(0001)_{\alpha'}$, which is 0.234 nm. We offer this as unequivocal evidence that the lattice parameter *a* of the C phase is 0.405 ± 0.003 nm. Measurements of the interplanar distances from multiple HAADF images were performed. According to the d-spacing of different planes measured from the C phase, the lattice parameter is measured within a range from 0.404 to 0.408 nm. Two examples are presented in Figs. 2a and 2b.

Although there is no FCC phase predicted in the equilibrium phase diagrams of Ti or in the Ti-6Al-4V system, there have been a series of reports of metastable FCC phases occurring in Ti alloys, stabilized by deformation, heating or the incorporation of other elements [2,3,12,41,42]. The lattice parameters of these FCC phases are summarised in Extended data Tab. S1 [2,3,12,42]. Some of these FCC phases were found to be hydrides or oxides of Ti that formed from the process of specimen preparation by electropolishing or focussed ion beam milling [2,12,42]. The lattice parameter of the C phase reported here (a = 0.406 nm) is clearly different from those hydrides or oxides of Ti (a ≥ 0.410 nm). Moreover, our specimens for EBSD analysis were prepared via mechanical polishing and our TEM foils were prepared using a precision ion polishing system at cryogenic temperature. These methods (described in detail in the supplementary materials) are known to reduce the possibility of the formation of hydride/oxide artefacts. The report of an FCC phase in pure Ti with a lattice parameter of a = 0.403 nm [4,13,42] is noteworthy

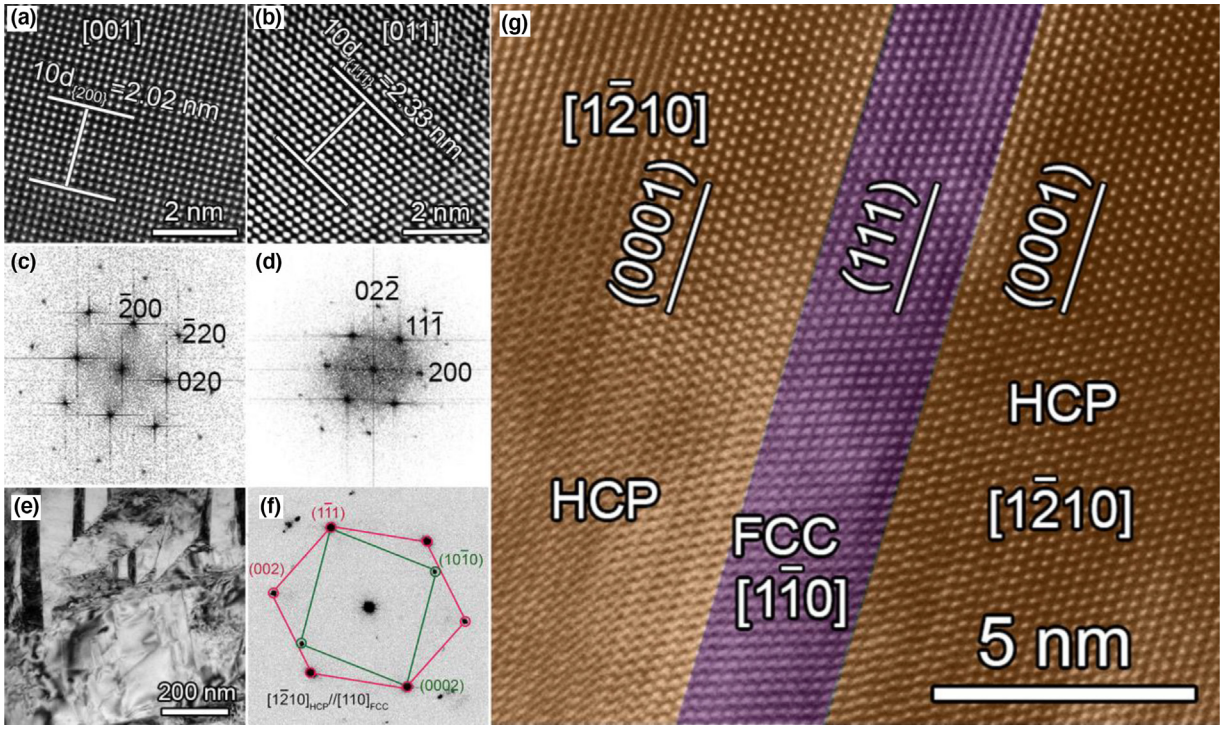

FIGURE 2

(a)–(b) STEM HAADF images recorded along the $\langle 0\,0\,1\rangle_C$ and $\langle 0\,1\,1\rangle_C$ zone axes, respectively. (c)–(d) The corresponding FFT of (a) and (b), respectively. (e) A bright-field TEM image recorded from a two-phase region revealing a high density of defects. (f) The corresponding SAED pattern to (e) recorded along the $\langle 1\,2\,\bar{1}\,0\rangle_{\alpha'}$ //$\langle 1\,\bar{1}\,\bar{1}\,0\rangle_C$ zone axis, indicating the orientation relationship between the two phases. (g) A STEM HAADF image recorded from a two-phase region along the $\langle 1\,2\,\bar{1}\,0\rangle_{\alpha'}$ //$\langle 1\,\bar{1}\,1\,0\rangle_C$ zone axis. Both the SAED pattern and the HAADF image reveal that $(0001)_{\alpha'}$//$\{111\}_C$.

as this value is close to our observation. In that work, the thin film sample was electrodeposited on an Al substrate. The metastable FCC phase was structurally and chemically stabilized by the templating effect of the FCC substrate.

A TEM dark-field image of a two-phase region is provided in Fig. 3a. STEM Energy dispersive X-ray spectroscopy (EDS) mapping was conducted in a dual-phase region (Extended data Fig. S2), revealing O atoms partition in FCC-phase regions. However, EDS analysis has limited sensitivity to light elements, resulting in poor quality of the resulting EDS maps. For quantitative chemical composition analysis, electron energy loss spectroscopy (EELS), and atom probe tomography (APT) experiments were conducted in the same sample region as that shown in Fig. 3a. STEM-EELS was used to analyze light elements in this region. Fig. 3b provides the EELS low-loss spectra, revealing a shift of the plasmon peaks from 17.1 eV in the α′ phase to 20.0 eV in the C-phase, as indicated by the two black arrows. Another edge at 10.6 eV was observed in the C-phase phase due to the different electronic structures between the two phases [43]. In the free electron Drude model [44], the plasmon energy E_P is proportional to the square root of the free electron density n, (i.e. $E_P \propto \sqrt{n}$). Therefore, an increase of the plasmon energy can be interpreted as an increase in the density of free electrons. Fig. 3c presents the high energy portion of the EEL spectrum. The intensity of the O edge (~532 eV) increased dramatically in the C phase, indicating that it is rich in oxygen. The concentration of O was calculated to be ~30.0 ± 5.0 at.% using the spectrum fitting of both low and high energy loss spectra (Extended data Tab. S2). This is much higher than that measured in the HCP phase (2.8 ± 1.0 at.%). Note that the measured O contents are expected to be higher than those normally reported in bulk materials because of the inevitable surface contamination in TEM specimens. Notwithstanding this, a significantly higher O concentration is evident in the C phase compared to the α′ phase. In fact, relative to the α′ phase, the C phase exhibited an L_3 Ti edge shift from 457.6 eV (α′) to 460.6 eV (C) and the L_2 Ti edge was shifted from 462.9 eV (α′) to 464.7 eV (C). Similarly, a V edge was observed with an edge shift from 514.8 eV (α′) to 516.9 eV (C). This is unequivocal evidence that the introduction of O changes the chemical bonding environment between the constituent atoms of the two phases. However, we suggest that the chemical bonding in the C phase remains predominantly metallic rather than (e.g.) covalent both because of the magnitude of the L_3 and L_3 Ti edge shifts, and the fact that O occurs in the EEL spectrum as a single peak rather than a double peak as is observed in Ti-O bearing compounds [45].

APT was used to study the changes in elemental distribution around the C-phase. Consistent with the EELS data, the results in Figs. 3d-e suggest a significant amount of O (maximum concentration = 32.9 ± 0.68 at. % to a 95% confidence interval) is partitioned to the C-phase. Our APT data also indicated a clear reduction in the concentration of H (Fig. 3e) in the (FCC) C phase relative to the surrounding (HCP) α′ matrix phase, further confirming that the C-phase is not a hydride phase. Minor concentrations (1–2 at.%) of H were detected in the two phases. However, this is background H that is always present in the atom

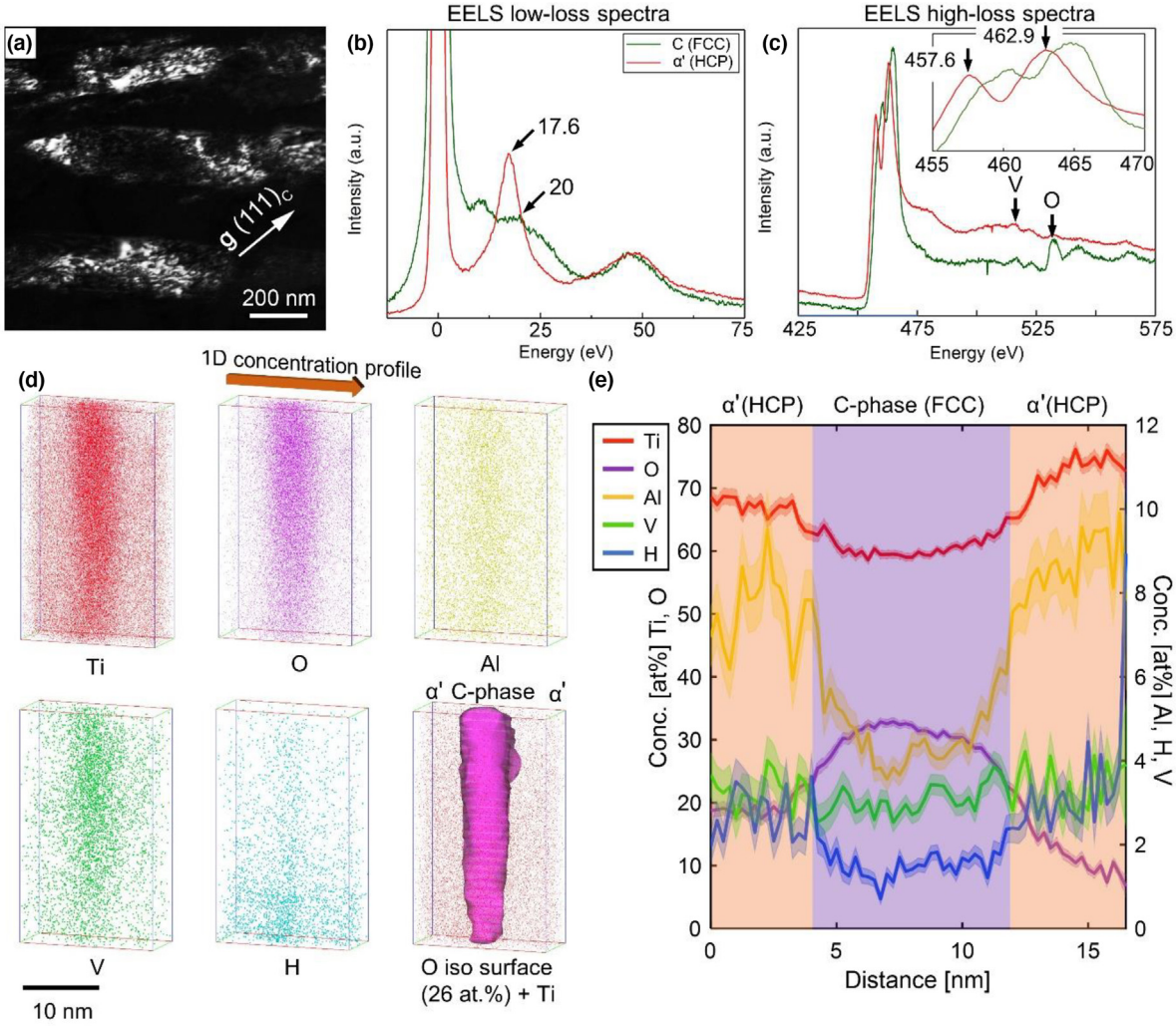

FIGURE 3

(a) A **g** (1 1 1)$_C$ TEM dark-field image recorded from a two-phase region. The lenticular morphology of the C (FCC) phase (bright contrast) is clealy apparent. In dark contrast is the α′ (HCP) phase. (b) and (c) provide STEM-EELS low-loss spectra and high-loss spectra, respectively. Red and green lines present the HCP α′ phase and the FCC C phase, respectively. (d) Tomographic atom maps of a region containing C-phase via APT. The bottom right shows an isoconcentraion surface (purple) of the C-phase region corresponding to 26 at.% O. (e) 1D concentration profiles of Ti, O, Al, H and V corresponding to the arrow indicated in the atom maps shown in (d) – the full volume of the region of interest was used for the profiles and the colours match those corresponding to the atom maps. The shaded error regions represent a 95% confidence interval of the profiles (bin width = 0.25 nm).

probe analysis chamber and does not originate from the specimen itself [46]. Detailed chemical composition of the C-phase is provided in the Extended data Table S3. The details of the APT tip reconstruction and the corresponding mass spectrum are provided in the Extended data Figs. S3 & S4.

DFT calculations

DFT calculations were performed to rationalize our observations [47]. The formation energy of interstitial O atom in the oxygen-bearing C phase was lower than that in the α′ phase, and preferably at the octahedral site (Extended data Tab. S4). To understand the distribution of O with respect to the C/α′ interphase interface, a layer-by-layer energy mapping was performed by adding one O interstitial to each layer across the interface, Fig. 4a. The layer-resolved relative energy profile is provided in Fig. 4b. Interestingly, there exists a slight barrier (~0.02 eV) close to the interface within the α′ phase (HCP) region. This barrier is thermally-sensitive, considering the Boltzmann energy at room temperature is approximately 0.025 eV [48]. These calculations indicate that O atoms prefer to reside at the octahedral sites of the C phase (FCC) structure over the α′ phase (HCP) by ~0.12 eV/atom.

A survey of the Ti-O phase diagram reveals that the only Ti-O containing phase with an FCC structure is cubic TiO (space group Fm3m, a = 0.423 nm) [49]. This is ~5% larger than the lattice parameter measured for the C phase and the difference of 0.02 nm would be discernable in our electron diffraction studies. Another consideration is the experimental compositional data which points to an O concentration of ~30-33 at.%, which is significantly far from the 50 at.% expected from the 1:1 stoichiometry of TiO. The nature of the occurrence of the O in the C-phase was assessed by inserting a pair of interstitial O atoms into a 108-atom supercell of a FCC Ti structure (a = 0.409 nm [50]), which is given in Extended data Fig. S5. The relative energy as a function

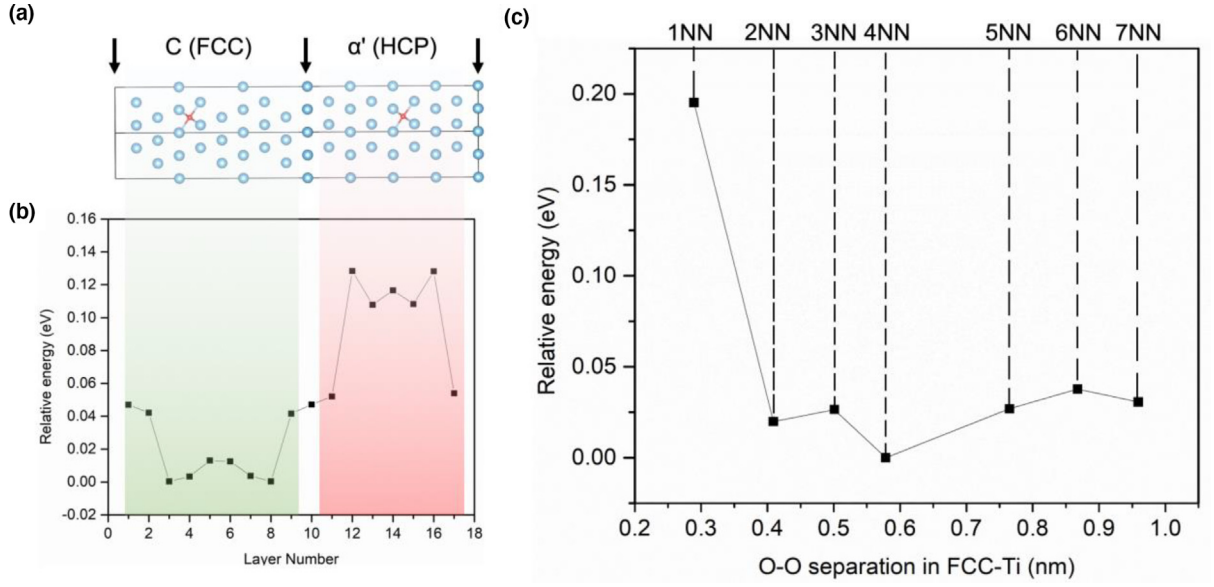

FIGURE 4

(a) A DFT FCC {1 1 1}/HCP {0 0 0 1} interface model with two octahedral interstitial O atoms at layer 4 and layer 14. The arrows indicate the FCC/HCP interfaces due to a periodic boundary condition. (b) The calculated layer-resolved relative energy mapping for an O atom throughout the model. (c) The calculated relative total energy of two O interstitial atoms in a 108-atom FCC-Ti supercell as a function of O pair separation.

of the pair separation is shown in Fig. 4c. These calculations indicate that the first nearest neighbour configuration (1NN) is highly unfavourable (by ~0.19 eV) compared to the higher order 2NN-7NN configurations, with the 4NN configuration being slightly favourable by ~0.025 eV, i.e. the Boltzmann energy at 300 K. This is further verified by simulating 14 O atoms in a large 256-atom supercell (Extended data Fig. S6). Collectively, these results suggest that the C phase is an interstitial solid solution where the O atoms are spaced at relatively higher order NN configurations, so as to avoid the relatively unfavourable 1NN arrangement.

Mechanical properties

The mechanical properties were evaluated via compression testing of polycrystalline micropillars. Three types of polycrystalline micropillars were investigated: a single-phase α′, single-phase C, and a two-phase region containing both α′ + C phases, each with ~50% volume fractions. As the mechanical properties of materials are sensitive to the grain orientation, we carefully selected HCP polycrystalline grains with a number of different orientations (Extended data Fig. S7 a), and prepared the FCC grains so that a ⟨1 0 0⟩ direction was parallel to the compression direction and a ⟨1 1 0⟩ direction was parallel to the electron beam direction (Extended data Figs. S7 b-c). The latter is for the convenience of TEM observation. With average dimensions of ~0.9 μm, over 20 randomly oriented α′ phase grains were included in each two-phase pillar. No less than 30 grains were included in each of the single-phase α′ phase pillars. In this way, the effects of grain orientation on mechanical properties were minimized. For micro-pillar compression tests, a transition in mechanical behaviour from bulk-like to size-dependant has been reported [51]. The interplay between external geometric size (the diameter of the micropillar) and grain size plays a critical role for the transition [51]. The external size determines the distance a dislocation glides before annihilation at the sample surface. The grain size, as a competing factor, alters the length of the mean free path of dislocations [51]. Theoretical research suggests that the sample size effect will be dominant when the ratio between the pillar diameter and the grain size is below a critical value of ~5 [51]. Experiments on irradiated copper pillars demonstrate strong sample size effects only when the sample diameter was smaller than ~400 nm [52]. The sample size effect on yield strength is reduced when the pillar size is in the micrometre regime and the resulting yield strength is close to that of the bulk [53]. In our study, the yield strength of the HCP micro-pillars (1.2 GPa) was only slightly higher than that of the bulk samples (1.1 GPa). Indeed the difference was less than 10%, indicating that the size effect was not significant in our study. As all the micro-pillars have similar dimensions, we suggest that the size effect on the yield strength of the FCC and dual-phase pillars was negligible. The significant enhancement of the local yield strength introduced by the C phase was reproducible.

True stress–strain (compression) curves from the pillars containing the α′ phase, the C phase and both the α′ + C phases are provided in Fig. 5a. Their corresponding compression properties are summarized in the Extended data Tab. S5. The pillars containing both phases demonstrated the highest compressive strength (1.9 ± 0.1 GPa yield strength). The C phase (1.7 ± 0.1 GPa yield strength) is stronger than the α′ phase (1.2 ± 0.1 GPa yield strength) but exhibits lower plasticity. The relatively low plasticity could be due to the sliding of twin boundaries, which has been frequently observed in the deformation of single-crystal FCC materials [54]. However, the plasticity of α′ + C phase pillars remains about the same value as the single-phase α′ phase pillars, indicating the introduction of the C phase does not lower the plasticity of the material.

To explore the deformation mechanisms of the dual-phase micropillars, cross-sectional TEM specimens were prepared to

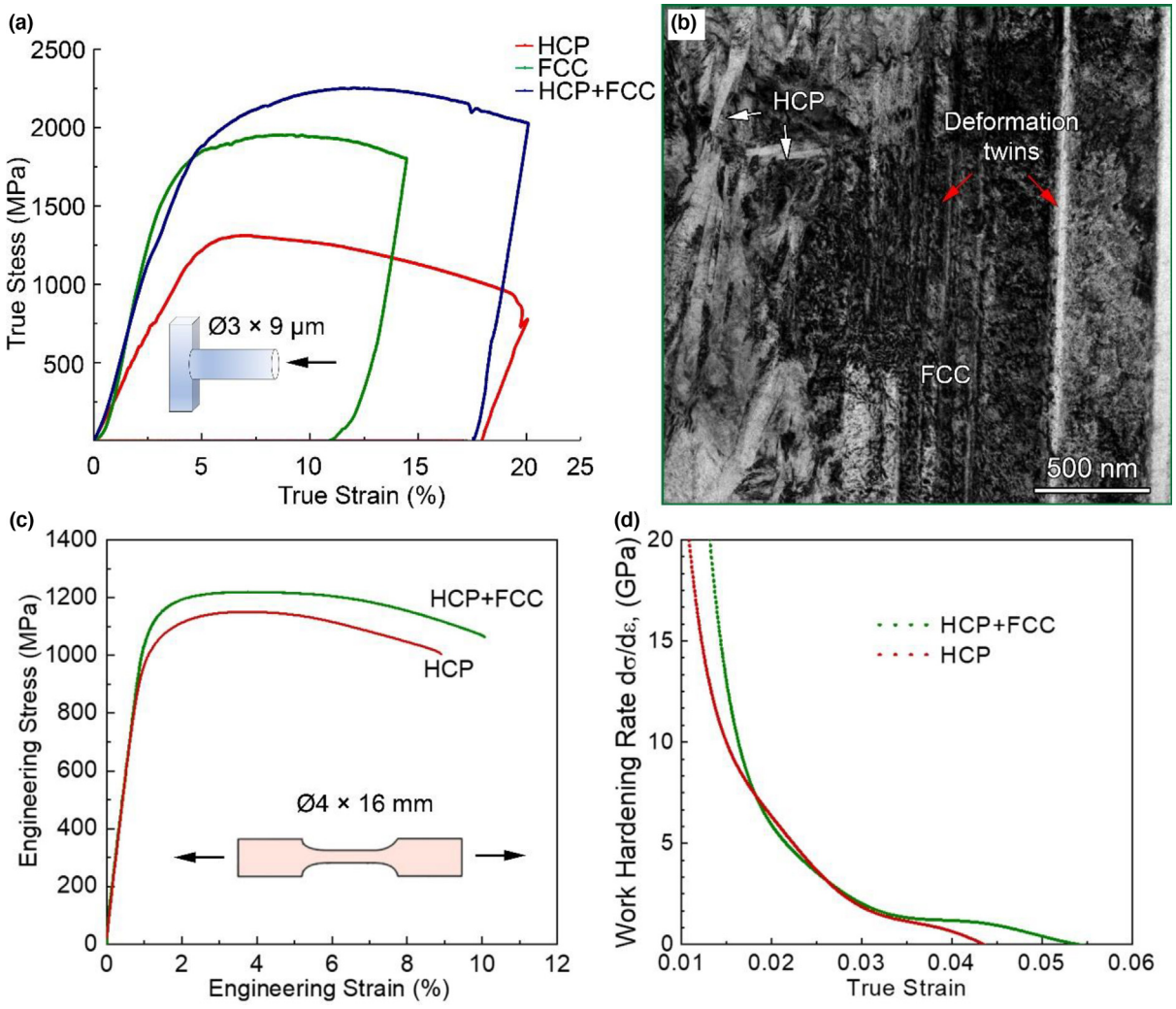

FIGURE 5

(a) Typical true compression stress–strain curves recorded from micro-pillars prepared from each phase and a 50/50 mix of the two phases. A schematic diagram of the specimen dimensions for the in-situ compression test is provided, inset. (b) A bright-field image of a deformed (0.2 true strain) two phase region. Two white arrows point to the needle-like HCP phase. A high density of dislocations and deformation twins (two of which are identified explicitly by red arrows) are evident in the C phase. (c) Engineering tensile stress–strain curves of bulk samples printed as coupons for tensile testing with dimensions provided in the inset. (d) The corresponding strain hardening rates.

investigate a deformed micro-pillar from a two-phase region. High densities of dislocations and deformation nanotwins were observed in the C phase region (Fig. 5b). The nanotwins (e.g. red arrows) possess an average thickness of ~60 nm.

Similar tensile results were also observed in the bulk samples subjected to tensile testing, Fig. 5c. To effect a valid comparison, the L-PBF printing parameters were adjusted so as to build samples that contained either only the α′ phase, or a mixture of α′ + C phases. Details of the printing parameters and microstructural characterization are discussed below. The average width and length of the acicular platelets of the α′ phase-only sample was ~1.0 μm and 10.5 μm, respectively. The grain size is comparable to those of α′ phase observed in the dual-phase sample. The martensitic Ti-6Al-4V containing the C phase represents a relatively high yield strength of 1113 ± 15 MPa, and a high ultimate tensile strength of 1221 ± 9 MPa, which is ~13% and 6% higher than the α′ alloy samples, respectively. Significantly, the sample containing both α′ and C phase exhibited greater ductility and work hardening capacity (Fig. 5d) with a uniform elongation and fracture strain of ~5.5 and 10 %, respectively. This compares with a uniform elongation and fracture strain of ~3.7 and 8.9 %, respectively, in the sample containing the α′ phase only. Extended data Fig. S8 presents a HRTEM image recorded from a dual-phase region in a fractured sample. A high density of dislocations exists in an area close to the interphase boundary, which should result in high levels of work hardening. A quantitative evaluation of the dislocation density near the phase boundary (10^{16} m^{-2}) is one order of magnitude higher than that observed in single phase regions. To avoid artefacts generated from inverse FFT images, dislocations near the edge of the images and in the fuzzy regions were not counted.

Discussion

Formation mechanism of the FCC phase

The O-rich nature of the FCC phase and its orientation relationship with the HCP phases suggest a possible two-step formation

mechanism: (i) formation of unstable FCC nuclei via plastic deformation of the HCP phase in a heterogeneously deformed (or O-enriched) regime due to the cyclic thermal loadings in the L-PBF process, and (ii) stabilization of the FCC nuclei via the diffusion (or pre-existence) of O into the FCC phase, facilitated by deformation induced defects and layer-by-layer reheating.

Deformation-induced HCP to FCC phase transformations in physical metallurgy often lead to specific orientation relationships [40,55]. For the orientation relationship $\langle 1\bar{2}10\rangle_{HCP}$ //$\langle 110\rangle_{FCC}$ and $(0001)_{HCP}$//$\{111\}_{FCC}$, the transformation usually occurs via successive gliding of Shockley partials on every other basal plane of the HCP phase [40,55]. Almost certainly, that mechanism is operating here. In the L-PBF process, the inherent high cooling rates result in the formation of a prevailing martensitic microstructure in the as-built state, which is composed of supersaturated fine α′ laths with a high dislocation density. It has been reported that O-bearing pure titanium can transform from HCP to FCC phase upon heating to 600 °C [3]. In titanium alloys, the passivation breaks down at temperatures ≥600 °C, enabling rapid diffusion of O from the oxide surface layer into the matrix. In the current study, the feedstock Ti-6Al-4V powder had a relatively higher O content than conventional wrought materials of 0.1 wt.%, compared to the more usual value of 0.01 wt.% [56]. The melting of spatter particles can also lead to local O-enrichment. During the L-PBF process, the layer-by-layer melting process can cause heat accumulation [32,57], resulting in parts of the build experiencing temperature excursions into the α + β phase region [32]. In the two-phase sample prepared with a 30 μm layer thickness, considerable amounts of β phase were also observed in the bottom regions (Extended data Fig. S9), indicating that the increase in temperature exceeded 600 °C [32]. This heating enhances the diffusion of O, which we propose promotes the formation of the FCC structured C phase. Meanwhile, the APT results (Fig. 3d) indicate that the V content in C phase is similar to the surrounding α′ grains, indicating the formation of C phase is isolated from the α′ to α + β decomposition process during intrinsic thermal activations.

In order to confirm the effect of heat accumulation, the microstructure of another L-PBF built specimen was characterized by EBSD for comparison. Detailed processing parameters are given in Extended data Tab. S6. Owing to the larger component size and higher laser power, the overall heat accumulation in this build is expected to be less, resulting in a lower thermal gradient. This was consistent with the observed microstructure, which was dominated by α′ and no C phase was detected (Extended data Fig. S10). The chemical composition of the as-built samples possessed similar O contents (0.1 wt.%) in both L-PBF samples [32]. This suggests that the relatively high O content and martensitic transformation do not induce the formation of the FCC phase without sufficient intrinsic thermal activation to facilitate O diffusion. Meanwhile, dislocation densities in the two samples were analyzed using X-ray diffraction (Extended data Fig. S11). The dislocation density was 1.48×10^{15} m^{-2} and 3.16×10^{15} m^{-2} in the low thermal gradient builds containing only the α′ phase and the high thermal gradient builds containing a mixture of α′ + C phases, respectively. We suggest that thermal stress induced plastic deformation led to the formation of unstable FCC nuclei in the lower thermal gradient builds such that the α′ to C transformation could not proceed. The partitioning of O was likely accelerated by dislocation pipe diffusional pathways [58,59]. Schematic diagrams are given in Extended data Fig. S12, presenting the two-step formation mechanism of the C phase.

Mechanical properties

A comparison of the mechanical properties measured from micro-pillars containing the dual α′ + C phases, the single C phase, and the single α′ phase demonstrates that the O solid solution strengthened C phase enhances the strength of the alloy significantly (Fig. 5a). An intense hardening effect from dilute oxygen solutes was reported by Yu *et al.* [34] in pure α-Ti (HCP) and this was proposed to be due to interactions between the O atoms and screw dislocations. The observed strengthening effect of the C phase confirms that this FCC phase is effective in strengthening titanium alloys and that this occurs by significant dislocation activity and nanotwinning (Fig. 5b). Indeed, these deformation microstructures are consistent with other FCC materials with ~20–25 mJm^{-2} stacking fault energy [60,61]. Previous studies have indicated that HCP metallic materials usually undergo work softening during deformation because of the lack of slip systems [62]. This is consistent with our in-situ compression results on micro-pillars of the α′ phase. When the C phase was introduced, work hardening did occur during compression via deformation twinning, dislocation interactions, and the interactions between dislocations and twin boundaries (Fig. 5b). It is well known that dynamic deformation twinning is an effective work hardening mechanism [63]. The higher maximum true stress achieved in the two-phase regions (2.3 GPa) over that measured in the single C phase regions (1.9 GPa) and the single α′ regions (1.3 GPa) indicates explicitly that the work hardening capability was improved significantly by the introduction of the HCP/FCC interphase interfaces [3].

Many factors will contribute to the mechanical strength of the alloy, including α′ lath thicknesses, dislocation density, twin density, and the volume fraction of each phase. The quantitative contribution of the C phase to the strengthening needs to be further investigated. We attribute the improved tensile ductility and work hardening capacity to the presence of the FCC phase formed at high temperature up to 600 °C. The reinforcing effect of the C phase in the Ti-6Al-4V alloy is very significant considering its low volume fraction (≤6.6%). We suppose that greater strengthening effects can be expected by increasing the volume fraction of the C phase in additively manufactured titanium alloys. Finally, our DFT results indicate that O atoms as solutes in the C phase opens a potential future pathway for exploiting alloying and processing conditions that increase the oxygen supersaturation, driving oxygen co-clustering reactions, and providing further potential for engineering the microstructure and further enhancing the mechanical properties of Ti alloys.

Conclusions

An oxygen-rich FCC phase, designated as C phase, has been discovered in a Ti-6Al-4V alloy produced by L-PBF. The C phase

exhibits a lattice parameter of 0.406 nm, an oxygen concentration of up to 33 at. % and an orientation relationship with the matrix α′ phase as follows: $(0001)_{\alpha'}//\{111\}_{C}$, and $\langle 1\bar{2}10\rangle_{\alpha'}//\langle 1\bar{1}0\rangle_{C}$. The significant thermal gradient, cyclic thermal loading, and incorporation of O during the L-PBF process are critical for the formation and stabilization of the C phase. The introduction of this FCC phase significantly benefits the mechanical properties of the material. The compression strength of pillars comprising near equal volume fractions of the FCC and the HCP phases was more than 70% higher than that of pillars comprising only the HCP phase, yet no loss in plasticity was measured. High densities of dislocations and deformation twins were observed in the deformed C phase, which is typical of deformed FCC structures with low stacking fault energy. Moreover, the HCP/FCC phase boundaries contribute to improve the mechanical properties. This research indicates that the mechanical properties of Ti-6Al-4V alloys prepared by AM and, more broadly other Ti alloys, may be significantly improved by the presence of the oxygen-stabilized FCC phase. We have demonstrated processing conditions whereby this phase can be deliberately introduced—the key parameters being the thermal gradient and the delivery of additional O via the feedstock materials to the additive manufacturing process.

Methods

Material processing and sample preparation. Gas atomized Ti–6Al–4V powder (ASTM Grade 23, ELI, 0.1 wt.% O, 0.009 wt.% N, 0.008 wt.% C, 0.17 wt.% Fe, <0.002 wt.% H; TLS Technik GmbH & Co.) in the particle size range of 25 – 45 μm was used. Two sets of samples with α′ martensite as the predominant microstructure were fabricated using an L-PBF facility (SLM Solutions GmbH, SLM 250 HL) with different printing parameters (Extended data Table S6). The specimens were processed using the same layer thickness (t = 30 μm) and hatch distance (h = 120 μm) but different laser power, scanning velocity and focal offset distance. This resulted in comparable volumetric energy densities (E) of melt pool in the range of 65–74 $J{\cdot}mm^{-3}$ but various overall thermal profiles due to the specimen size and processing parameters. The samples were vertically built on a Ti-6Al-4V substrate (pre-heated to 200 °C) with support structures [30]. Prior to L-PBF fabrication, the build chamber was purged with high-purity argon gas until the oxygen level was below 100 ppm. The as-built samples showed a near full-density of > 99.5% as measured by the micro-CT technique.

For cross-sectional observation in SEM, the as-built sample was cut using an Acctom-50 diamond saw along the build direction. Top layer and bottom layer samples were cut ~300 μm and ~20 mm away from the top surface, respectively. Specimens for SEM characterization were cut using an Acctom-50 diamond saw along the build direction, ground using diamond suspension with diamond grain sizes of 30, 15, 6, 3, and 1 μm and then polished using 0.05 μm oxide dispersion suspension. Specimens for TEM and TKD were sliced from a bottom layer of the cylinder, ground to a thickness of ~30 μm followed by ion milling using a Gatan model 691 precision ion polishing system at –50 °C, beam voltage of 4 kV and milling angle of ± 6°. APT specimens were prepared from the SEM specimens using the FIB-based lift-out method [64].

Structural characterization, in-situ micropillar compression and bulk dog-bone specimen tensile testing. EBSD and TKD experiments were conducted using a Zeiss Ultra SEM equipped with an EBSD detector. TEM characterization was performed using a Titan Themis-Z double-corrected microscope equipped with ChemiSTEM (Super-X) X-ray Energy-dispersive spectroscopy detectors and a Gatan Quantum ER/965 GIF dual EELS system. With the dual EELS system, energy alignment was performed to zero-loss peak, which makes the observed peak shifts reliable. EELS thickness mapping was conducted in the STEM mode to estimate the thickness effect of specimens. The formula used for the thickness measurements was $t = \lambda \ln(I_t/I_0)$, where t is the specimen thickness, λ is the mean free path of inelastic electron scattering with a value of 109.5 nm, and I_t and I_0 are the total and zero-loss intensities in the electron-energy loss spectrum, respectively [65]. Here, as reasonable approximation, the λ value is treated as a constant because the structural difference and O concentration have minor effects on the mean free path of inelastic electron scattering.

APT experiments were carried out in a laser-assisted CAMECA local electrode atom probe (LEAP) 4000X Si at a cryogenic temperature of ~50 K with a 355 nm wavelength laser, 90 mm straight flight path, with a pulse energy of ~20 pJ and a pulse frequency of ~200 kHz. The tomographic reconstruction was performed using CAMECA's Integrated Visualization & Analysis Software version 3.8.4. Tip radius was derived from the voltage evolution method. A detector efficiency of 57 % as previously calculated for this particular atom probe using methods referred to Refs. [38,39] was used. The default image compression factor (1.65), and k_f (3.30) were applied since no crystallographic information could be observed in the field evaporation maps. A representative mass spectrum and 1D concentration profile were exported and plotted in MATLAB.

In-situ micro-pillar compression tests were performed using a Hysitron PI-85 picoindenter in the displacement-control mode with a displacement rate of 2 nm/s or a strain rate of $\sim 2 \times 10^{-4}$-s^{-1}. All the pillars had similar dimensions of ~3 μm in diameter at the pillar top, ~9 μm in length, and ~3° tapering angle. It is expected that a large aspect ratio of length to diameter increases significantly the possibility of buckling while a small ratio results in unrealistic extra strain hardening [66]. Pillars with aspect ratios ranging 1:2–1:3 are recommended for micro-compression tests [66].

Cylindrical dog-bone shaped tensile specimens were machined with gauge dimensions of $\dot{A}4 \times 16$ mm proportional to ASTM standard E8/E8 M-09. Room temperature quasi-static uniaxial tensile testing was performed at an initial strain rate of 2.5×10^{-4} s^{-1} using an MTS 810 universal testing facility equipped with a 100 kN load cell and a non-contact laser extensometer. At least three samples with the same printing parameters were tested to get the mechanical properties. The true stress values were calculated by using the load and real time cross-sectional area from the middle height of the pillar. Because the yield strength and compression strength of HCP bulk sam-

ples were ~1.10 GPa [32] and ~1.25 GPa, respectively, which are about the same as those of the HCP pillars. This indicates little sample size effect on the measured mechanical properties of pillars for the dimensions used in this study.

DFT method. DFT calculations were performed using the generalized gradient approximation [67] with the Vienna Ab initio Simulation Package (VASP) code [68,69]. The cut-off energy for plane wave basis sets was 500 eV. Monkhorst-Pack k-points were meshed by 6 × 6 × 6 for the 108-atom bulk model and 6 × 6 × 1 for the interface model. For all systems, atomic relaxation was allowed until the forces were less than 0.01 eV/Å.

Considering the low concentrations of substitutional V and Al, and their relatively even contributions in the FCC and HCP phases, one can use pure Ti supercells to study the bulk and interface structures of Ti-6Al-4V. The formation energies of single interstitial O atom at the octahedral and tetrahedral sites were calculated in bulk HCP-Ti and FCC-Ti using 96-atom and 108-atom supercells, respectively. The formation energy is defined as $E_{super\text{-}with\text{-}O} - E_{pure\text{-}super} - ½ E_{O2}$, where $E_{super\text{-}with\text{-}O}$, $E_{pure\text{-}super}$ and E_{O2} are the energies of the supercell containing one O atom, the pure supercell, and oxygen molecule, respectively. A 2 × 2 in-plane 9-layer FCC (1 1 1)/ 8-layer HCP (0 0 0 1) fully coherent interface structure was constructed using a supercell with periodic boundary conditions to study the distribution of O with respective to the interface. The relaxed lattice constants of the interface supercell are a = 0.5819 nm and c = 3.9736 nm.

Author contributions

X.Z.L., S.P.R., Z.B.C., and W.X. conceived, designed, and led the project. H.W., Z.B.C, M.C. characterized microstructures. H. W. conducted the in-situ compression experiments in SEM. Q. C. performed mechanical testing of bulk samples and XRD experiments. Q.C. and W.X. selected the processing parameters and printed the samples. X.Y.C conducted DFT simulations. A.J.B conducted APT analysis and contributed to the writing of APT related parts of the manuscript. H.W. and Q.C. drafted the initial manuscript. All co-authors contributed to the data analysis and discussion.

Data and materials availability

All data needed to evaluate the conclusions in the paper are present in the paper and/or the Supplementary Information. Additional data related to this paper may be requested from the authors.

Data availability

Data will be made available on request.

Declaration of Competing Interest

The authors declare that they have no known competing financial interests or personal relationships that could have appeared to influence the work reported in this paper.

Acknowledgements

This project is supported by the Australia–US Multidisciplinary University Research Initiative (AUSMURI) program (3Dadditive.com.au). XZL was also supported by the Australian Research Council [DP190102243], WX by [DP150104719], SP by [DE180100440] and SPR by [DP200100940]. ZBC would like to express his sincere thanks for the financial support from the Research Office (Project code: P0041361 and P0039966) of The Hong Kong Polytechnic University. The authors acknowledge the scientific and technical input and support from Sydney Microscopy & Microanalysis—a core research facility of the University of Sydney and the University's node of Microscopy Australia. This research was undertaken with the assistance of the National Computational Infrastructure (NCI), and we acknowledge the expert support of the Sydney Informatics Hub at the University of Sydney in accessing these computational resources. Microscopy Australia and the NCI are supported by the Australian Government under the NCRIS program.

Appendix A. Supplementary material

Supplementary data to this article can be found online at https://doi.org/10.1016/j.mattod.2022.10.026.

References

[1] D. Banerjee et al., Acta Metall. 36 (1988) 125–141.
[2] R. Traylor et al., Acta Mater. 184 (2020) 199–210.
[3] Q. Yu et al., Scr. Mater. 140 (2017) 9–12.
[4] R. Banerjee, R. Ahuja, H.L. Fraser, Phys. Rev. Lett. 76 (1996) 20.
[5] R. Banerjee et al., Acta Mater. 47 (1999) 1153–1161.
[6] A.F. Jankowski, M.A. Wall, J. Mater. Res. 9 (1994) 31–38.
[7] Y. Yamada, Y. Kasukabe, K. Yoshida, Jpn. J. Appl. Phys. 29 (1990) 706–709.
[8] D.L. Zhang, D.Y. Ying, Mater. Lett. 52 (2002) 329–333.
[9] D.V.A.N. Heerden, Acta Metall. Inc. 44 (5) (1996) 297–306.
[10] R. Sarkar et al., Philos. Mag. Lett. 94 (2014) 311–318.
[11] Y. Chang et al., Nat. Commun. 10 (2019) 1–10.
[12] Y. Chang et al., Scr. Mater. 178 (2020) 39–43.
[13] R. Banerjee, S.A. Dregia, H.L. Fraser, Acta Mater. 47 (1999) 4225–4231.
[14] J. Kim, E. Plancher, C.C. Tasan, Acta Mater. 188 (2020) 686–696.
[15] H. Conrad, Prog. Mater Sci. 26 (1981) 123–403.
[16] Y. Zheng et al., Scr. Mater. 152 (2018) 150–153.
[17] S. Gorsse et al., Sci. Technol. Adv. Mater. 18 (2017) 584–610.
[18] Y.M. Wang et al., Nat. Mater. 17 (2018) 63–70.
[19] Z.G. Zhu et al., Scr. Mater. 154 (2018) 20–24.
[20] L. Liu et al., Mater. Today 21 (2018) 354–361.
[21] Y. Kok et al., Mater. Des. 139 (2018) 565–586.
[22] C. Kamath et al., Int. J. Adv. Manuf. Technol. 74 (2014) 65–78.
[23] D. Herzog et al., Acta Mater. 117 (2016) 371–392.
[24] T. Voisin et al., Mater. Des. 158 (2018) 113–126.
[25] D. Zhang et al., Nature 576 (2019).
[26] Z. Lei et al., Nature 563 (2018) 546–550.
[27] P.C. Collins et al., Mater. Sci. Eng., A 352 (2003) 118–128.
[28] G. Welsch, R. Boyer, E.W. Collings, Materials Properties Handbook: Titanium Alloys, ASM International, 1993.
[29] J.W. Elmer et al., Mater. Sci. Eng., A 391 (2005) 104–113.
[30] W. Xu et al., Acta Mater. 125 (2017) 390–400.
[31] G. Welsch et al., Metall. Trans. A 8 (1977) 169–177.
[32] W. Xu et al., Acta Mater. 85 (2015) 74–84.
[33] Y. Chang et al., Acta Mater. 150 (2018) 273–280.
[34] Q. Yu et al., Science 347 (2015) 635–639.
[35] Q. Wang et al., Acta Mater. 183 (2020) 329–339.
[36] J.-E. Sundgren et al., Thin Solid Films 105 (1983) 367–384.
[37] B. Vrancken et al., J. Alloy. Compd. 541 (2012) 177–185.
[38] R. Nesper, Angew. Chem.Int. Ed. English 30 (1991) 789–817.
[39] M. Yan et al., Powder Metall. 57 (2014) 251–257.
[40] H. Zhao et al., Acta Mater. 131 (2017) 271–279.
[41] D.H. Hong et al., Scr. Mater. 69 (2013) 405–408.
[42] R. Banerjee, Thin Films: Structural Transitions, Dekker Encyclopedia of Nanoscience and Nanotechnology, Taylor & Francis, 2014.
[43] Y. Kihn, C. Mirguet, L. Calmels, J. Electron. Spectros. Relat. Phenom. 143 (2005) 117–127.
[44] R.F. Egerton, Electron Energy-Loss Spectroscopy in the Electron Microscope, Springer US, Boston, MA, 2011.
[45] C. Zhang et al., npj Quantum Mater. 2 (2017).

[46] R.P. Kolli, Adv. Struct. Chem. Imaging 3 (2017) 1–10.
[47] X.Y. Cui, S.P. Ringer, Mater. Charact. 146 (2018) 347–358.
[48] S.K. Nayak et al., npj Comput. Mater. 4 (2018).
[49] J.L. Murray, H.A. Wriedt, J. Phase Equilibria 8 (1987) 148–165.
[50] H.C. Wu et al., Sci. Rep. 6 (2016) 1–8.
[51] W. Liu et al., Phys. Rev. Lett. 124 (2020) 1–7.
[52] D. Kiener et al., Nat. Mater. 10 (2011) 608–613.
[53] D. Kiener, C. Motz, G. Dehm, Mater. Sci. Eng., A 505 (2009) 79–87.
[54] Z.J. Wang et al., Nat. Commun. 8 (2017) 1–7.
[55] H. Zhao et al., Scr. Mater. 132 (2017) 63–67.
[56] Y.G. Ko et al., Scr. Mater. 54 (2006) 1785–1789.
[57] P. Kürnsteiner et al., Nature 582 (2020) 515–519.
[58] M. Fiebig et al., Science 319 (2008) 1646–1650.
[59] Q. Ding et al., Acta Mater. 154 (2018) 137–146.
[60] Q. Lin et al., Mater. Res. Lett. 6 (2018) 236–243.
[61] H. Wang et al., Acta Mater. 196 (2020) 609–625.
[62] W.B. Hutchinson, M.R. Barnett, Scr. Mater. 63 (2010) 737–740.
[63] Y.T. Zhu, X.Z. Liao, X.L. Wu, Prog. Mater. Sci. 57 (2012) 1–62.
[64] K. Thompson et al., Ultramicroscopy 107 (2007) 131–139.
[65] K. Iakoubovskii et al., Microsc. Res. Tech. 71 (2008) 626–631.
[66] M.D. Uchic et al., Science 305 (2004) 986–989.
[67] L. Liu et al., Mater. Charact. 157 (2019) 109898.
[68] G. Kresse, J. Furthmüller, Comput. Mater. Sci. 6 (1996) 15–50.
[69] D. Joubert, Phys. Rev. B - Condens. Matter Mater. Phys. 59 (1999) 1758–1775.